Heterodoped Nanotubes: Theory, Synthesis, and Characterization of Phosphorus–Nitrogen Doped Multiwalled Carbon Nanotubes

Eduardo Cruz-Silva,[†] David A. Cullen,[‡] Lin Gu,[‡] Jose Manuel Romo-Herrera,[†] Emilio Muñoz-Sandoval,[†] Florentino López-Urías,[†] Bobby G. Sumpter,[§] Vincent Meunier,[§] Jean-Christophe Charlier,[⊥] David J. Smith,[‡] Humberto Terrones,[†] and Mauricio Terrones[†,*]

[†]Advanced Materials Department, IPICyT, Camino a la Presa San José, 2055, San Luis Potosí 78216, México, [‡]School of Materials and Department of Physics, Arizona State University, Tempe, Arizona 85287, [§]Oak Ridge National Laboratory. P.O. Box 2008, Oak Ridge, Tennessee 37831-6367, and [⊥]Université Catholique de Louvain, PCPM & ETSF, B-1348 Louvain-la-Neuve, Belgium

ABSTRACT Arrays of multiwalled carbon nanotubes doped with phosphorus (P) and nitrogen (N) are synthesized using a solution of ferrocene, triphenyl-phosphine, and benzylamine in conjunction with spray pyrolysis. We demonstrate that iron phosphide (Fe_3P) nanoparticles act as catalysts during nanotube growth, leading to the formation of novel PN-doped multiwalled carbon nanotubes. The samples were examined by high resolution electron microscopy and microanalysis techniques, and their chemical stability was explored by means of thermogravimetric analysis in the presence of oxygen. The PN-doped structures reveal important morphology and chemical changes when compared to N-doped nanotubes. These types of heterodoped nanotubes are predicted to offer many new opportunities in the fabrication of fast-response chemical sensors.

KEYWORDS: multiwalled carbon nanotubes · chemical vapor deposition · doping · electronic structure

Carbon nanotubes (CNT)[1,2] have attracted the attention of numerous research groups because of their outstanding mechanical and electronic properties. For example, carbon nanotubes can potentially be used as reinforcement for composite fabrication,[3] as components in nanoscale integrated circuits,[4] or as supports for catalytic particles.[5] The cylindrical shape of carbon nanotubes leads to novel properties that are not present in bulk graphite, such as the ability to behave as a metal or as a semiconductor depending on the tube chirality and diameter.[6,7] The nanotube curvature changes the chemically inert graphite surface and makes it easier to incorporate atoms on the tube surface. In this context, nitrogen, which is known to have low doping levels in bulk graphite,[8] can be easily incorporated into carbon nanotubes by substitution. Inclusion of noncarbon atoms into the hexagonal network of carbon nanotubes modifies the electronic and chemical properties due to variations in electronic structure. Nitrogen, for example, acts as an electron donor in a carbon nanotube since it has five valence electrons, causing a shift in the Fermi level to the valence bands, and hence making all N-doped tubes metallic, regardless of their geometry.[9] Nitrogen can also be incorporated within nanotubes in a pyridine-like fashion. It is noteworthy that the doped sites within carbon nanotubes significantly modify chemical reactivity, thereby broadening the spectrum of possible applications.[9]

Although phosphorus atoms are larger than carbon atoms, it has been shown that phosphorus can form substitutional defects in diamond sp^3 thin films, behaving as an n-type donor and thereby modifying the electronic and optical properties.[10] Theoretical work has also shown that carbon tetragons containing phosphorus are stable in CP_x sp^2 cage-like structures and that phosphorus atoms promote large curvature when incorporated into sp^2-like fullerene structures.[11] Growth of carbon nanotubes in the presence of phosphorus has been previously reported.[12] In that case, phosphorus was incorporated in the catalytic particles before synthesis, either by using an anodic alumina substrate (which has an inherent phosphorus contamination due to its production process) or by treating an alumina substrate with phosphoric acid and then using it as a support for iron/nickel particles. It was found that the nanotubes were sequentially grown (matchstick-like)

*Address correspondence to mterrones@ipicyt.edu.mx.

Received for review October 28, 2007 and accepted February 14, 2008.

Published online March 7, 2008.
10.1021/nn700330w CCC: $40.75

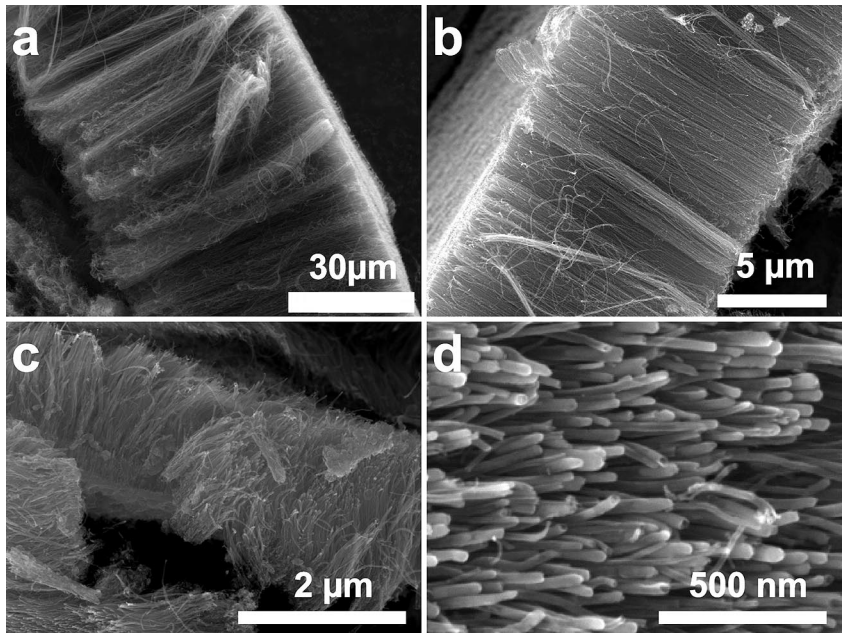

Figure 1. Scanning electron micrographs of PN-doped carbon nanotube (CNT) arrays, synthesized at the optimum temperature and carrier gas flow rate, and different TPP concentrations: (a) pristine N-doped CNTs (sample A); (b) 2.5 wt % TPP (sample B); (c) 3.3 wt % TPP (sample C); (d) substrate side of a PN-CNT mat (sample B).

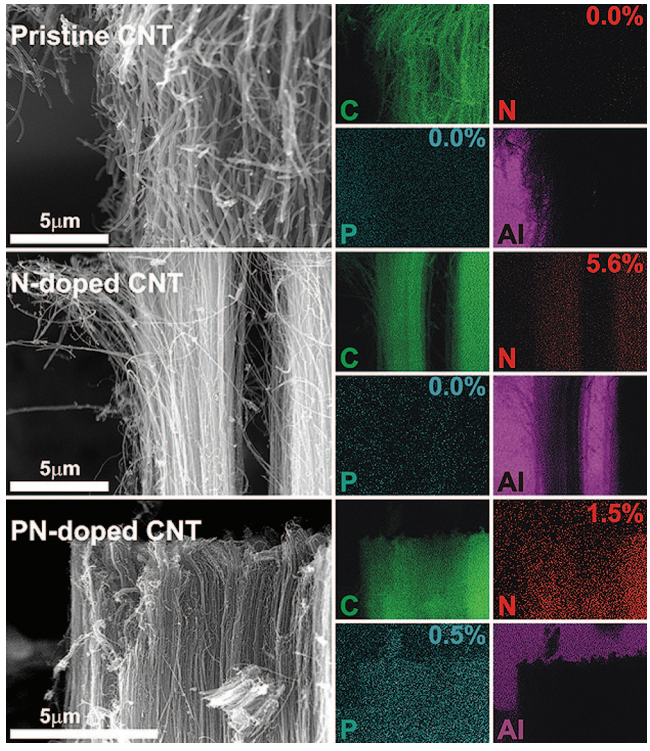

Figure 2. EDX elemental mappings for three different types of nanotubes: pristine pure carbon nanotubes (CNTs) obtained by thermolazing toluene ($C_6H_5-CH_3$) and ferrocene at 850 °C (see top frame); N-doped CNTs described in the Materials and Methods section (see middle frame), and PN-doped CNTs described in the Materials and Methods section (see bottom frame). Samples were mounted on standard aluminum pins to have contrast for the carbon map. It can be clearly observed that the PN-sample contains both phosphorus and nitrogen in their structure, thus confirming the successful synthesis of PN heteroatomic doping. The other samples did not show heteroatomic doping.

and that the catalytic particles were composed of a metal phosphide.[12] An optimum set of experimental conditions were later identified to increase the yield of these types of nanotubes, but whether phosphorus was incorporated in the hexagonal nanotube lattice was never discussed.[13]

In the present work, we address the theory of PN-doped carbon nanotubes as well as their successful synthesis by thermolysis of hydrocarbons and a floating catalyst method. The growth of these nanotubes is catalyzed by iron phosphide particles. We show unequivocally for the first time that P and N are indeed chemically incorporated within the nanotube lattice.

RESULTS AND DISCUSSION

The first step in this work was to find the optimal synthesis conditions at which PN-doped nanotubes are grown. To do this, two sets of experiments were performed. In the first, a solution with 2.5 wt% of triphenyl-phosphine (TPP) and 7.5% of ferrocene dissolved in benzylamine (see Materials and Methods section for more details) was pyrolyzed for 20 min inside a furnace operated at fixed temperature, ranging from 720 to 840 °C in increments of 40 °C, and the Ar flow varied from 0.8 to 1.6 L/min. It was found that the only conditions capable of producing nanotube materials occurred at 760 and 800 °C with an Ar flow of 0.8 L/min; and a higher yield of nanotubes occurred at the lower temperature. In the second set of experiments, the temperature was set to 760 °C and the concentration of ferrocene dissolved in benzylamine was set to 7.5 wt %, while the concentration of the P dopant (TPP) was varied, using 0, 2.5, and 3.3 wt %.

For scanning electron microscopy (SEM) analysis, we selected samples where the concentration of the phosphorus dopant was varied. It was observed that for a given synthesis temperature, and by increasing the phosphorus content in the solution, a reduction in the yield of carbon nanotubes occurred. SEM images confirmed that samples consisted mainly of highly ordered arrays of multiwalled carbon nanotubes (MWCNTs), with very low content of amorphous carbon. The nanotube length is also reduced as the P content in the solution is increased: in the absence of phosphorus the nanotubes are *ca.* 70 μm long (sample A, Figure 1a), but the nanotube length is reduced to *ca.* 12 μm (sample B, Figure 1b) when 2.5 wt% of TPP is added to the spray solution. For experiments with 3.3 wt % of TPP, the length of the nanotubes observed was *ca.* 2~3 μm

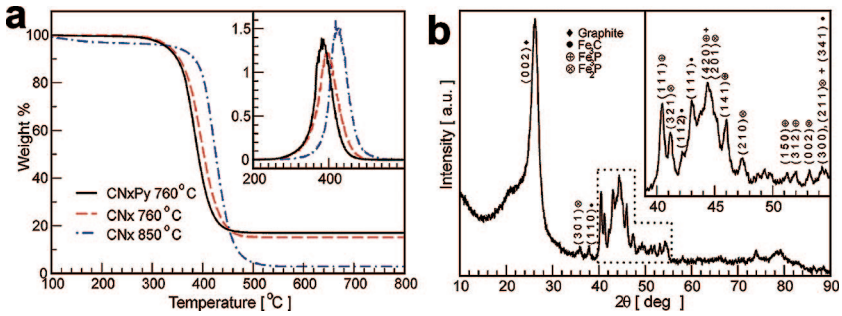

Figure 3. (a) Thermogravimetric analysis of N-CNT and PN-CNT. The latter are oxidized at lower temperature, indicating higher chemical reactivity. The larger amount of byproducts for lower temperature nanotubes is a consequence of a higher proportion of metal particles as a result of shorter nanotubes. The inset shows that the oxidation onset for PN-CNT occurs 15 °C below the onset for N-CNT grown under the same conditions. (b) X-ray diffraction pattern of PN-doped CNTs (sample B). The inset shows enlargement of the region between 40 and 55°. The metal particles in the sample are a mixture of Fe_3C, Fe_2P, and Fe_3P. The mean particle sizes are 10∼12, 13, and 17 nm, respectively.

(sample C, Figure 1c), and the disorder within the nanotube arrays was significantly increased. After these observations, sample B was chosen as the work sample on the basis of its higher nanotube yield. The substrate side of the nanotube mats (Figure 1d) shows that most of the nanotubes have either a metal particle in the carbon nanotube base or a hole left by a missing particle. Note that these metal particles are rarely observed on the opposite side. This is consistent with a base growth model, as previously reported for N-doped nanotubes grown using the same synthesis method.[14] It was noticed that neither sequential nor tip growth could be observed as a consequence of phosphorus inclusion during the synthesis, as previously reported by Jourdain *et al.*[12]

Elemental maps from N-doped and PN-doped carbon nanotubes as well as a pristine nanotube control sample were obtained by EDX spectroscopy on the SEM (Figure 2). The samples were mounted on aluminum pins, and their corresponding map is presented. The instrument was able to detect traces of nitrogen in the N-doped case. In the case of PN-doped nanotubes, it is clear that both phosphorus and nitrogen are present in the entire sample. Quantification of the EDX spectra obtained in these nanotubes is shown in the maps, confirming very low levels of P doping (0.5 atom %) for the PN-doped case.

Thermogravimetric analysis (TGA; Figure 3a) provides information suggesting that the presence of phosphorus reduces the temperature for oxidation (*i.e.*, the tubes appear to be more reactive). In this case, we compared the oxidation of N- and PN- doped nanotubes grown at the optimum conditions. We first noted that samples synthesized at lower temperatures (*e.g.*,, 760 °C) have higher amounts of metal oxide byproducts after oxidation because the mass of material that did not burn corresponded to *ca.* 17–20%. This is because a higher proportion of metal to carbon was found since the nanotubes were much shorter. The inset of Figure 3a shows the derivative of the normalized weight *versus* temperature. When comparing the TGA data for N-doped samples only, we could attribute the 20 °C shift in the oxidation onset temperature to the higher amounts of N within the tubes produced at low temperature, thus making the tubes more reactive. However, addition of phosphorus makes a further shift of 15 °C toward lower temperatures. Given the remarkable absence of amorphous carbon and the cleanliness of the sample, this shift indicates a higher chemical re-

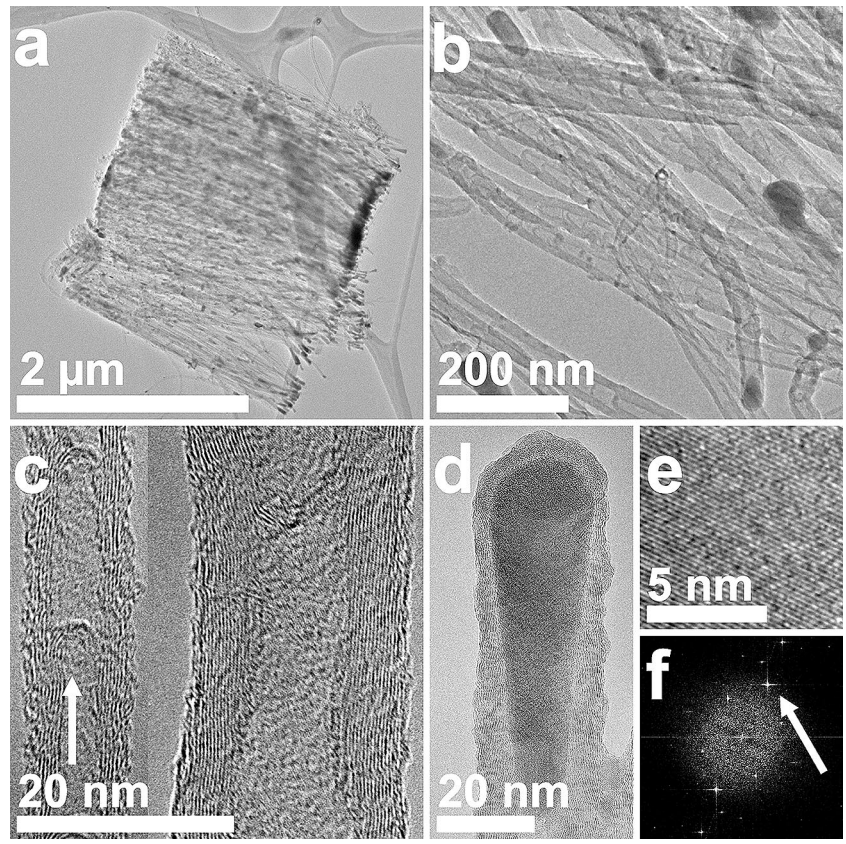

Figure 4. TEM and HRTEM images of PN-doped CNT (sample B). Low-resolution TEM (a,b) shows the position of metal particles inside CNTs, and their overall morphology. The degree of crystallinity can be observed in nanotube walls (c) and tips (d). High-resolution images of the metal particle at the tip (e), and its Fourier transform (f), show lattice planes with a separation of 1.97Å corresponding to (141) plane for Fe_3P.

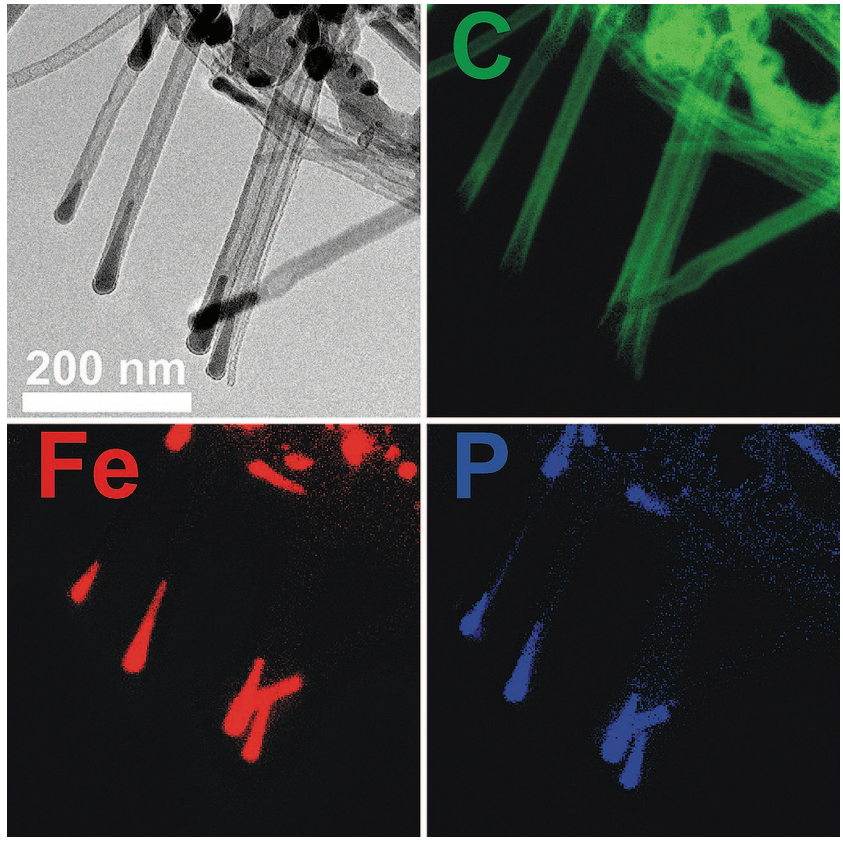

Figure 5. EELS elemental mapping of PN-doped CNTs (sample B). Most of the metal particles consist of Fe_xP, with some exceptions (Fe only, top right of each frame). Phosphorus content in the nanotube walls is below the EELS detection threshold, and therefore the phosphorus mapping on the tube walls becomes noisy.

activity for the heteroatomic PN-doped carbon nanotubes when compared to the N-doped nanotube sample produced under the same experimental conditions.

To understand the role of phosphorus and its relation to iron during the growth of this type of nanotube, X-ray powder diffraction studies were performed on a sample synthesized with 2.5 wt % of TPP (see Figure 3b). The bulk diffraction pattern shows a combination of two phases of iron phosphide (Fe_2P and Fe_3P) in addition to iron carbide (Fe_3C, bainite). The main peak in the diffraction pattern is due to the (002) reflection of graphite, which is characteristic of multiwalled carbon nanotubes. The peaks located between 40 and 50° (see inset of Figure 3b) are due to a combination of reflections arising from Fe_2P, Fe_3P and Fe_3C (indicated in Figure 3b). The major peak in this region is the sum of the (111) reflections from Fe_3C, (420) from Fe_3P, and (201) from Fe_2P. When analyzing nonoverlapping peaks from the XRD spectra, it was found that the mean particle size for Fe_3P was close to 17 nm [calculated using Scherrer's equation with the full width at half-maximum (fwhm) of peaks (111) and (141)]; note that these values are in agreement with the Fe_3P particle sizes observed by TEM (see Figure 4). For the (301) and (210) reflections of Fe_2P, the mean particle size was found to be close to 13 nm, and for the Fe_3C (111) and (112) reflections, the mean size was estimated as 10∼12 nm.

To develop a better understanding of the composition and growth process, we analyzed the nanotubes and the catalytic metal particles by high resolution electron microscopy (HRTEM). It is noteworthy that PN-doped nanotubes are less stable under the electron beam than their N-doped counterparts, visibly degenerating after shorter exposure times. Low-resolution TEM images (Figure 4a,b) confirm that most of the catalytic particles are located on one side of the nanotube mat, and that these are composed mainly of bamboo-shaped nanotubes. Good crystallinity can be observed in some nanotube walls (see Figure 4c), but they are less ordered in the regions close to the metal particles (Figure 4d), and in the bamboo compartments (as indicated by an arrow on Figure 4c). Most of the catalytic metal nanoparticles appear to be single crystal, and high-resolution images show interplanar distances that match those of Fe_3P. The particle diameter observed by TEM was *ca.* 20 nm, close to the mean value of 17 nm obtained from X-ray powder diffraction data. The lattice planes of a metal particle are clearly visible in Figure 4e. The clear spot in the Fourier transform of this image (see arrow on Figure 4f) indicates the strong periodicity of these planes, with a separation of 1.97 Å, which corresponds closely to the (141) interplanar spacing of Fe_3P. Other crystallographic planes were not easily found aligned perpendicular to the electron beam direction.

From energy filtered imaging, we find that most of the catalytic particles are primarily composed of Fe and P (see Figure 5). Some particles exhibit small amounts of oxygen at the ends of the nanotube tips due to oxidation (images not shown here). It was observed that some metallic particles (usually covered by amorphous-like carbon) do not contain phosphorus (see top right of each frame in Figure 5); these are probably iron or iron carbide (note that Fe_3C is present in the X-ray powder diffraction pattern, see Figure 3b). The

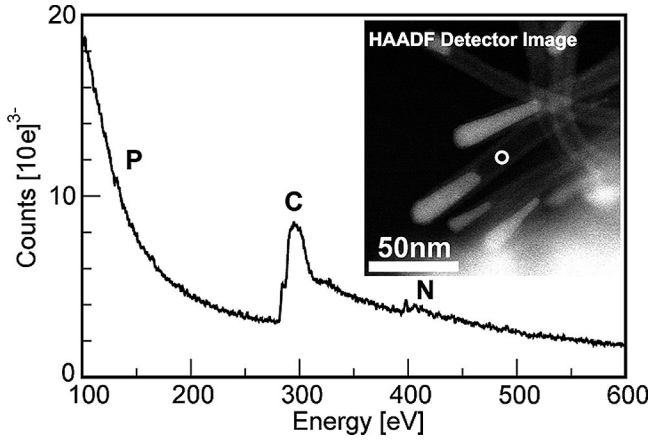

Figure 6. EELS spectrum of an individual PN-doped nanotube (see marked region in the HAADF image inset). The carbon edge is very intense, while small concentrations of both phosphorus and nitrogen can be seen in the spectrum; these peaks are masked by the plural scattering background (for P) and by the intense carbon edge (for N).

phosphorus content within the nanotube walls is below the EELS detection threshold, and thus it could not be clearly observed by elemental mapping. However, an EEL spectrum of PN-doped nanotubes (Figure 6) shows an intense carbon edge at 285 eV, as well as small peaks that correspond to phosphorus (ionization edge at *ca.* 130 eV) and nitrogen (ionization edge at *ca.* 400 eV). The inset of Figure 6 shows the high angular annular dark field image (HAADF) of the nanotube used to obtain this spectrum. It is important to note that the phosphorus signal was strongly masked by the plural scattering background, whereas the nitrogen signal was masked by the tail of the carbon edge. This masking effect results in noisy EELS maps for N and P. However, Figure 2 clearly shows an EDX map that demonstrates

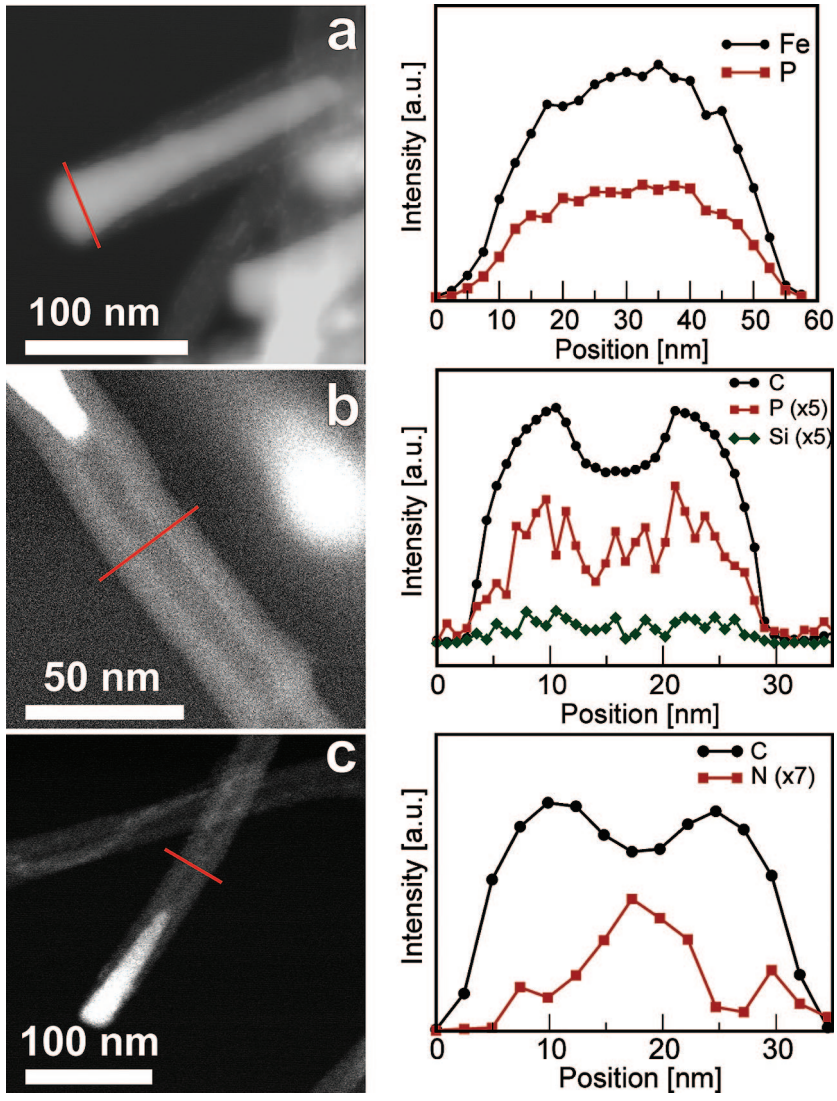

Figure 7. STEM elemental line-scans of individual PN-doped CNTs (sample B) using EDX (a) and EELS (b, c). Quantification of the EDX spectrum in metal nanoparticles confirms that their composition is Fe_3P. EEL spectra provide evidence of phosphorus doping in the nanotube walls, as well as the presence of gaseous N inside bamboo chambers and small amounts of N in the walls.

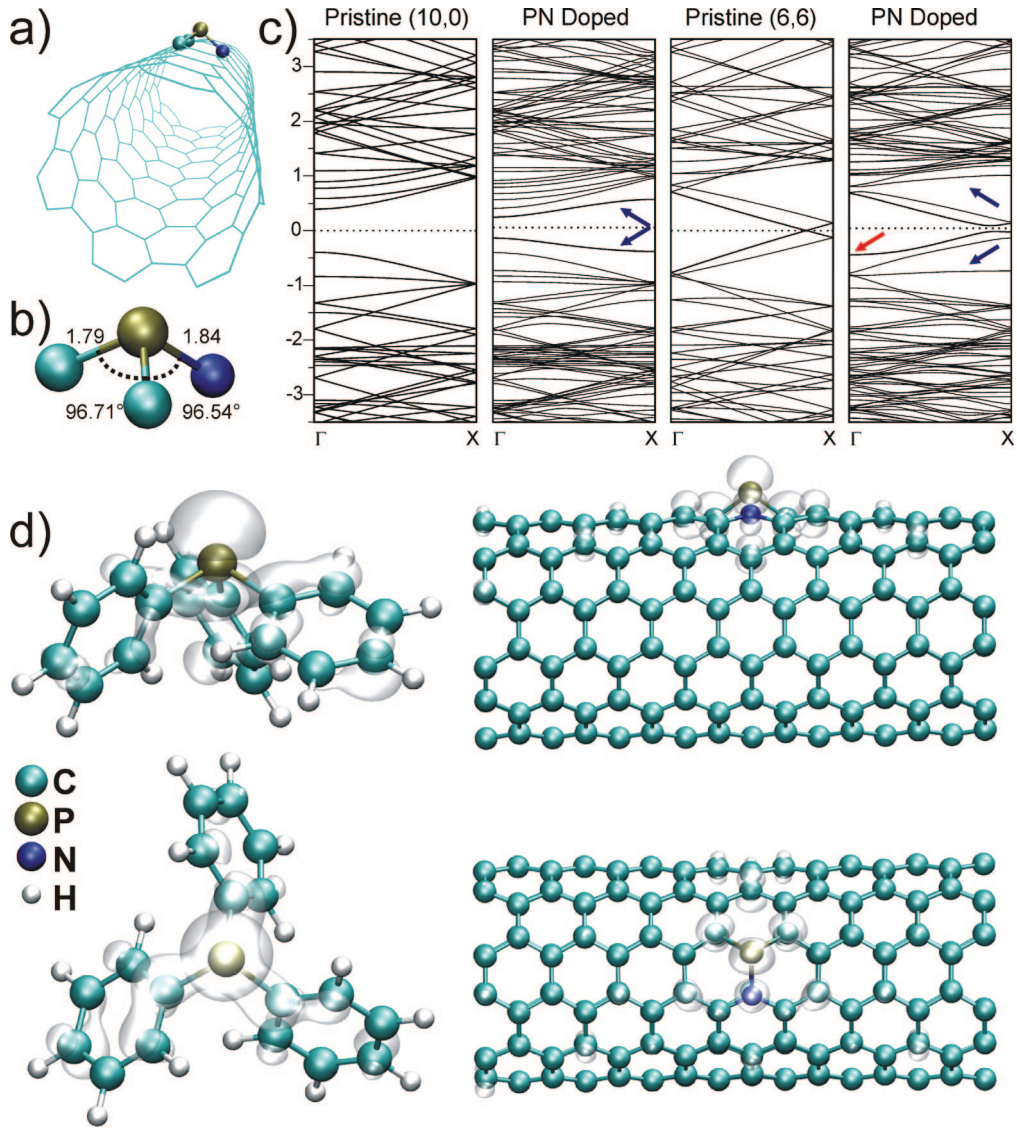

Figure 8. (a) Molecular model of a (6,6) PN-doped carbon nanotube with the hexagonal carbon network drawn as wires; (b) detail of the defect with information of the bond lengths and angles; (c) band structure for PN-doped (10,0) and (6,6) nanotubes compared with pristine (pure carbon) nanotubes; the effects of the doping are indicated by arrows; (d) charge density plots of the top valence band in the Γ-point for a (6,6) nanotube and comparison with the HOMO of triphenylphosphine.

the presence of P, N, and C within the nanotubes. EDX line profiles reveal a homogeneous composition within the metal particle (Figure 7a), and quantitative analysis indicates a stoichiometry close to 3:1 for Fe to P, in agreement with the HRTEM image analysis corresponding to Fe_3P. All catalytic particles analyzed by EDX spectroscopy were this phase of iron phosphide. It is noteworthy that Fe_3C and Fe_2P particles were not observed in the carbon nanotube tips. Note that Fe_2P particles were not found in the nanotube tips because Fe_2P does not dissolve C at this temperature. Therefore, Fe_2P is not responsible for the nanotube growth. EELS line scans in the nanotube region close to the catalytic particle indicate that the carbon nanotube has a homogeneous distribution of phosphorus, which has a weak signal that follows the profile of carbon (see Figure 7b). To rule out possible noise effects originating from the overlapping of the inelastic scattering peak with the phosphorus signal, the silicon signal (*ca.* 30 eV lower than phosphorus) was also integrated. It can be seen that while the integrated Si signal has a value close to zero, the integrated P signal increases and decreases together with the C signal. This indicates low but homogeneous doping of phosphorus within the carbon nanotube. Although the TEM images show bamboo-shaped nanotubes, which is a characteristic of N-doped nanotubes,[9,14,15] EELS was only able to detect N traces within the nanotube walls due to the dominating signal of the C edge that masks the N edge. However, N was clearly detected in the gaseous phase within the bamboo compartments; a feature observed only in N-doped tubes (see Figure 7c).[14]

From extensive simulations of the stability and electronic structure of PN-doped carbon nanotubes using

first principles calculations, we found that PN-doped nanotubes, having P and N as first neighbors, exhibited lower binding energy than PN-doped nanotubes with noncontiguous dopants. A model representation of these nanotubes is shown in Figure 8a. Further details regarding the electronic structure of the various nanotubes are beyond the scope of the present paper, and will be published elsewhere.[16] Here, we limit our discussion only to the PN-doped case. As can be observed in Figures 8a and 8b, the P atom is pushed outward upon structural relaxation, extending P−C and P−N bonds from 1.44 to 1.79 Å for P−C bonds and 1.84 Å for P−N bonds, and the tube diameter increases from 8.3 to 9.3 Å at the P site. The bond angles consequently change from 119° to 96.54° for C−P−N and 96.71° for C−P−C, which correspond to a tetragonal bonding typical of sp^3 P, very close to the 98° value of TPP. The additional electrons of P and N thus create localized states around the defect (blue arrows), as well as hybridization of the top valence band close to the γ-point in the (6,6) case (red arrow), as indicated in Figure 8c. The charge density associated with this state in a(6,6) nanotube is plotted in Figure 8d, and compared with the highest occupied molecular orbital (HOMO) of TPP. Note that the presence of a band gap in the PN-doped (6,6) nanotube is an artifact of the supercell method. It can be observed that the spatial distribution of this nanotube orbital is very similar to that of the HOMO of triphenylphosphine, suggesting that it could have similar chemical behavior, enabling carbon nanotubes to bind to atoms such as oxygen, sulfur, or chlorine.

CONCLUSIONS

In summary, we have successfully synthesized P- and N-doped carbon nanotubes by a CVD method, using benzylamine and triphenylphosphine as nitrogen and phosphorus sources, respectively. Results obtained from TGA show that these tubes have lower oxidation temperature when compared to N-doped nanotubes. A dramatic reduction in the yield of carbon nanotubes is observed as the TPP concentration is increased. This is a consequence of the reduction of nanotube length, which suggests reduced catalytic activity for iron phosphide when compared to pure iron. The heteroatomic doped nanotubes obtained by this method are highly ordered, and grew from their root (substrate). EDX and EELS elemental maps and profiles confirmed that phosphorus and nitrogen are homogenously incorporated into the nanotubes. Some iron particles are visible in the elemental mapping, and X-ray diffraction measurements show that there is iron carbide present in the sample. However, EDX and EELS spectroscopy indicate that most of the catalytic particles are composed of iron phosphide. Using *ab initio* electronic structure calculations, it is shown that P and N can coexist as dopants in carbon nanotubes and that a PN defect is the most stable of the studied configurations. The ternary phase diagram of carbon−iron−phosphorus[17] shows a metastable boundary between Fe_3C and Fe_3P at 700 °C, with an eutectic point close to 966 °C for 12.8 atom % of carbon in Fe_3P. However, there is no stable or metastable boundary reported for Fe_2P and Fe_3C at the synthesis temperature range used in this study. If carbon nanotubes grow from supersaturated Fe_3C, as shown recently,[18] it is possible to form this compound at the surface of Fe_3P while it is dissolving carbon, but not in Fe_2P. This would explain why the yield of carbon nanotubes is reduced with increased phosphorus content in the feedstock solution.

MATERIALS AND METHODS

Synthesis. For the synthesis process, a solution composed of benzylamine $C_6H_5-CH_2-NH_2$ (Sigma 99%) as carbon and nitrogen sources, ferrocene $Fe(C_5H_5)_2$ (Sigma, 98%) as catalyst and triphenyl-phosphine $P(C_6H_5)_3$ (TPP) (Sigma, 99%) as the phosphorus source was atomized using an aerosol generator and carried by an inert gas flow (argon) inside a quartz tube with an inner diameter of *ca.* 24 mm, which was placed inside a two-stage furnace system. This spray pyrolysis technique is similar to that described by Pinault *et al.*[19] and Kamalakaran *et al.*[20] The nanotubes were collected from the soot deposited on the surface of the quartz tube in the region located inside the furnace.

Characterization. The samples as synthesized were characterized by X-ray powder diffraction (Brucker Advance D8), thermogravimetric analysis (Thermo Corp. Cahn Versatherm HS, 1.5 g/0.1 μg), and scanning electron microscopy (FEI XL30-FEG 30 kV). For high resolution transmission electron microscopy (JEOL 4000EX HRTEM, operated at 400 kV) and scanning transmission electron microscopy (Philips CM200, Tecnai F20 with GIF, JEOL 2010), the samples were mounted on a copper grid with holey carbon coating after dispersion in isopropanol.

Electronic Structure Calculations. To complement the experimental evidence and to understand the relationship between phosphorus and nitrogen as dopants, we performed total energy electronic structure calculations for pristine, N-doped, P-doped, and PN-doped metallic (6,6) and semiconducting (10,0) nanotubes, consisting of 192 and 200 atoms, respectively. The electronic structure calculations were performed using density functional theory[21,22] within the local spin density approximation (DFT-LSDA) using the Ceperley−Alder parametrization[23] as implemented in the code SIESTA.[24] The wave functions were represented by a linear combination of pseudoatomic valence orbitals using a double-ζ polarized basis (DZP),[25] while core–electrons were represented by norm-conserving Troullier−Martins pseudopotentials in the Kleynman−Bylander nonlocal form.[26,27] The real-space grid used for charge and potential integration is equivalent to a planewave cutoff energy of 150 Ry. Periodic boundary conditions were used and the intertube distance was kept to a minimum of 10 Å to avoid lateral interactions. Given the system size, sampling of the 1D Brillouin zone with eight *k*-points was enough to converge the wave functions. The total energy was calculated when the forces were converged to less than 0.02 eV/Å.

Acknowledgment. Authors are grateful to D. Ramírez, G. Ramírez, L. Noyola, and G. Pérez Assaf for technical assistance. This work was supported in part by CONACYT-México grants 56787 (Laboratory for Nanoscience and Nanotechnology Research-LINAN), 45762 (H.T.), 45772 (M.T.), 41464-Inter American Materials Collaboration (M.T.), 42428-Inter American Materials Collaboration (H.T.), 2004-01-013/SALUD-CONACYT (M.T.), PUE-2004-CO2-9 Fondo Mixto de Puebla (M.T.) and Ph.D. schol-

arships (E.C.S. and J.M.R.H.), as well as NSF Grant DMR-0303429 (D.J.S.). V.M. and B.G.S. acknowledge work supported by the Center for Nanophase Materials Sciences (CNMS), sponsored by the Division of Scientific User Facilities, U.S. Department of Energy and by the Division of Materials Science and Engineering, U.S. Department of Energy under Contract No. DEAC05-00OR22725 with UT-Battelle, LLC at Oak Ridge National Laboratory (ORNL). Computations were performed using the resources of the National Center for Computational Sciences at ORNL. J.-C.C. is indebted to FNRS of Belgium for financial support. Parts of this work are also directly connected to the Belgian Program on Interuniversity Attraction Poles (PAI), to the ARC sponsored by the Communauté Française de Belgique, and to the NANOQUANTA and FAME European Networks of Excellence. We acknowledge use of facilities within the John M. Cowley Center for High Resolution Electron Microscopy at Arizona State University.

REFERENCES AND NOTES

1. Oberlin, A.; Endo, M.; Koyama, T. Filamentous Growth of Carbon Through Benzene Decomposition. *J. Cryst. Growth* **1976**, *32*, 335–349.
2. Iijima, S. Helical Microtubules of Graphitic Carbon. *Nature* **1991**, *354*, 56–58.
3. Ajayan, P. M.; Stephan, O.; Colliex, C.; Trauth, D. Aligned Carbon Nanotube Arrays Formed by Cutting a Polymer Resin-Nanotube Composite. *Science* **1994**, *265*, 1212–1214.
4. Tans, S. J.; Verschueren, A. R. M.; Dekker, C. Room-Temperature Transistor Based on a Single Carbon Nanotube. *Nature* **1998**, *393*, 49–52.
5. Plainex, J. M.; Coustel, N.; Coq, B.; Brotons, V.; Kumbhar, P. S.; Dutartre, R.; Genese, P.; Bernier, P.; Ajayan, P. M. Application of Carbon Nanotubes as Supports in Heterogeneous Catalysis. *J. Am. Chem. Soc.* **1994**, *116*, 7935–7936.
6. Saito, R.; Fujita, M.; Dresselhaus, G.; Dresselhaus, M. S. Electronic Structure of Graphene Tubules Based on C_{60}. *Phys. Rev. B* **1992**, *46*, 1804–1811.
7. Hamada, N.; Sawada, S.; Oshiyama, A. New One-Dimensional Conductors: Graphitic Microtubules. *Phys. Rev. Lett.* **1992**, *68*, 1579–1581.
8. Nozaki, T.; Yazawa, K. The Radioactivation Analysis of Graphite for Nitrogen by the $^{14}N(p,\alpha)\,^{11}C$ Reaction. *Bull. Chem. Soc. Jpn.* **1964**, *37*, 1891–1892.
9. Terrones, M.; Jorio, A.; Endo, M.; Rao, A. M.; Kim, Y. A.; Hayashi, T.; Terrones, H.; Charlier, J.-C.; Dresselhaus, G.; Dresselhaus, M. S. New Direction in Nanotube Science. *Mater. Today* **2004**, *7* (10), 30–45.
10. Sternschulte, H.; Thonke, K.; Sauer, R.; Koizumi, S. Optical Evidence for 630 meV Phosphorus Donor in Synthetic Diamond. *Phys. Rev. B* **1999**, *59*, 12924–12927.
11. Gueorguiev, G. K.; Furlan, A.; Högberg, H.; Stafström, S.; and Hultman, L. First Principles Calculations on the Structural Evolution of Solid Fullerene-Like CP_x. *Chem. Phys. Lett.* **2006**, *426*, 374–379.
12. Jourdain, V.; Stéphan, O.; Castignolles, M.; Loiseau, A.; and Bernier, P. Controlling the Morphology of Multiwalled Carbon Nanotubes by Sequential Catalytic Growth Induced by Phosphorus. *Adv. Mater.* **2004**, *16*, 447–453.
13. Jourdain, V.; Paillet, M.; Almairac, R.; Loiseau, A.; and Bernier, P. Relevant Synthesis Parameters for the Sequential Catalytic Growth of Carbon Nanotubes. *J. Phys. Chem. B* **2005**, *109*, 1380–1386.
14. Reyes-Reyes, M.; Grobert, N.; Kamalakaran, R.; Seeger, T.; Golberg, D.; Rühle, M.; Bando, Y.; Terrones, H.; Terrones, M. Efficient Encapsulation of Gaseous Nitrogen Inside Carbon Nanotubes with Bamboo-Like Structure Using Aerosol Thermolysis. *Chem. Phys. Lett.* **2004**, *396*, 167–173.
15. Sumpter, B. G.; Meunier, V.; Romo-Herrera, J. M.; Cruz-Silva, E.; Cullen, D. A.; Terrones, H.; Smith, D. J.; and Terrones, M. Nitrogen-Mediated Carbon Nanotube Growth: Diameter Reduction, Metallicity, Bundle Dispersability, and Bamboo Formation. *ACS Nano* **2007**, *1*, 396–375.
16. Cruz-Silva, E.; López-Urías, F.; Sumpter, B. G.; Meunier, V.; Terrones, H.; Terrones, M. Unpublished work.
17. C-Fe-P Phase Diagram. In *Handbook of Ternary Alloy Phase Diagrams*; Villars, P., Prince,A., Okamoto, H., Eds.; ASM International: Materials Park, OH, 1995; Vol. 5, pp 6786–6793..
18. Rodriguez-Manzo, J. A.; Terrones, M.; Terrones, H.; Kroto, H. W.; Sun, L.; Banhart, F. *In Situ* Nucleation of Carbon Nanotubes by the Injection of Carbon Atoms into Metal Particles. *Nat. Nanotechnol.* **2007**, *2*, 307–311.
19. Pinault, M.; Mayne-L'Hermite, M.; Reynaud, C.; Pichot, V.; Launois, P.; Ballutadud, D. Growth of Multiwalled Carbon Nanotubes During the Initial Stages of Aerosol-Assisted CCVD. *Carbon* **2005**, *43*, 2968–2976.
20. Kamalakaran, R.; Terrones, M.; Seeger, T.; Kohler-Redlich, P.; Rühle, M.; Kim, Y. A.; Hayashi, T.; Endo, M. Synthesis of Thick and Crystalline Nanotube Arrays by Spray Pyrolysis. *Appl. Phys. Lett.* **2000**, *77*, 3385–3387.
21. Hohenber, P.; Kohn, W. Inhomogeneous Electron Gas. *Phys. Rev.* **1964**, *136*, B864–B871.
22. Kohn, W.; Sham, L. J. Self-Consistent Equations Including Exchange and Correlation Effects. *Phys. Rev.* **1965**, *140*, A1133–A1138.
23. Ceperley, D. M.; Alder, B. J. Ground State of the Electron Gas by a Stochastic Method. *Phys. Rev. Lett.* **1980**, *45*, 566–569.
24. Soler, J. M.; Artacho, E.; Gale, J. D.; García, A.; Junquera, J.; Ordejón, P.; Sánchez-Portal, D. The *Siesta* Method for Ab Initio Order-N Materials Simulation. *J. Phys.: Condens. Matter* **2002**, *14*, 2745–2779.
25. Junquera, J.; Paz, O.; Sánchez-Portal, D.; Artacho, E. Numerical Atomic Orbitals for Linear-Scaling Calculations. *Phys. Rev. B* **2001**, *64*, 235111.
26. Troullier, N.; Martins, J. L. Efficient Pseudopotentials for Plane-Wave Calculations. *Phys. Rev. B* **1991**, *43*, 1993–2006.
27. Kleinman, L.; Bylander, D. M. Efficacious Form for Model Pseudopotentials. *Phys. Rev. Lett.* **1982**, *48*, 1425–1428.